

A Possible Formation Scenario for Dwarf Spheroidal Galaxies – I: Fiducial Model

P. Assmann^{1,2} \star , M. Fellhauer¹ \dagger , M.I. Wilkinson³ \ddagger , R. Smith¹ \S

¹ *Departamento de Astronomía, Universidad de Concepción, Casilla 160-C, Concepción, Chile*

² *Departamento de Astronomía, Universidad de Chile, Camino El Observatorio 1515, Las Condes, Santiago, Chile*

³ *Department of Physics & Astronomy, University of Leicester, University Road, Leicester LE1 7RH, UK*

30 October 2018

ABSTRACT

We use numerical simulations to study a formation scenario for dwarf spheroidal galaxies in which their stellar populations are the products of the dissolution of open star clusters and stellar associations within cosmological dark matter haloes. This paper shows that this process gives rise to objects which resemble the observed dwarf spheroidal satellites of the Milky Way without invoking external influences. The presence of long-lived kinematic substructures within the stellar components of these objects affects their projected velocity dispersions. We find that this in turn affects mass estimates based on the projected velocity dispersion profiles which may over-estimate the actual dark matter halo mass depending on the amount of substructure which is present. Our models make predictions about the detailed kinematic and photometric properties of the dSphs which can be tested using future observations.

Key words: galaxies: dwarfs — galaxies: star clusters — methods: N-body simulations

1 INTRODUCTION

Dwarf spheroidal galaxies (dSph) galaxies are believed to be the most dark matter (DM) dominated stellar systems known. They have low stellar content and are poor in, or entirely devoid of, gas. They are widely thought of as the smallest cosmological structures containing DM in the Universe (Mateo 1998; Lokas 2009; Walker et al. 2009) and are regarded as key objects in the formation of larger galaxies. According to the Λ -CDM cosmological model, complex structures are formed hierarchically (Read et al. 2006) in the potential wells of DM haloes, having density distributions following a Navarro, Frenk & White (NFW) profile (Navarro et al. 1997). The dSph galaxies would be formed first in small haloes, and then become involved in the mechanisms of forming larger, complex objects.

The dSph galaxies are characterized by absolute magnitudes in the range $-13 \leq M_V \leq -9$ (Mateo 1998; Belokurov et al. 2007). Their total estimated masses, considering both the stars and the DM halo, is of the order of $10^7 M_\odot$ to $10^8 M_\odot$, within their half-light radii. With the advent of the Sloan Digital Sky Survey (SDSS York et al. 2000), many new faint and ultra-faint dSph galaxies were detected around the Milky Way (MW) (e.g. Willman et al. 2005; Belokurov et al. 2006; Zucker et al. 2006; Belokurov et al. 2007; Walsh et al. 2007, and many more). Many of these dwarfs

are less luminous than a globular cluster (or even an open cluster) yet they exhibit high velocity dispersions (given their luminous mass) (e.g. Simon & Geha 2007; Koch et al. 2009; Geha et al. 2009) and, similarly to the so-called “classical” dSphs, are not rotationally supported (Gebel et al. 2003). Should these objects be in virial equilibrium, they are the most dark matter (DM) dominated objects known in the universe. They would exhibit mass-to-light (M/L) ratios of more than a thousand (e.g. Simon & Geha 2007; Fellhauer et al. 2008; Geha et al. 2009).

Recent works have demonstrated that dSph galaxies are DM dominated objects (Kleyna et al. 2002, 2003, 2004; Munoz et al. 2005, 2006; Walker et al. 2007; Simon & Geha 2007). They have observed that the stellar velocity dispersion of the classical dSphs is of the order of 10 km s^{-1} and that it remains approximately constant with distance from the centre of the galaxy.

There are several models that attempt to explain the origin of dSph galaxies by considering different mechanisms. Some of them are based on tidal and ram-pressure stripping (Mayer et al. 2007; Gnedin et al. 1999). In these models, the dSph galaxies are formed due to the interaction between a rotationally supported dwarf irregular galaxy and a MW-sized host galaxy. These models show that dSph galaxies tends to appear near a spiral galaxy, but they do not explain the presence of distant isolated dSph galaxies, such as Tucana and Cetus. The model proposed by D’Onghia et al. (2009) considers a mechanism known as resonant stripping and can be used to explain the formation of isolated dSph galaxies. Basically, these objects are formed after encounters between dwarf disc galaxies and larger systems, in a process driven by gravitational resonances. There is another model that explains the formation of dwarf

\star E-mail: passmann@astro-udec.cl

\dagger mfelhauer@astro-udec.cl

\ddagger miw6@astro.le.ac.uk

\S rsmith@astro-udec.cl

galaxies based on energy and momentum conservation when gas-rich galaxies interact (Metz et al. 2007). In this model the dSph galaxies are regarded as second-generation objects, devoid of DM, forming in the tidal tails of gas-rich interacting galaxies. All the models cited above consider the interaction between two or more galaxies to explain the formation of dSph galaxies.

There are models which consider dwarf galaxies in isolation (Valcke et al. 2008; Revaz et al. 2009) but they usually take only a smooth gas distribution into account and/or focus on higher masses for the dwarfs. Sawala et al. (2010), for example, perform cosmological re-simulations of dwarf haloes in the mass-range 2.3×10^8 to $1.1 \times 10^9 M_\odot$ using an SPH code with a star formation recipe. Where the density of the gas is sufficiently high (amongst other, more sophisticated criteria to mimic a correct global star formation), they convert gas particles into star particles, having masses of about 10^2 to $10^3 M_\odot$. They do not take into account, that those masses in stars would form in an association or in a small dissolving cluster, because it is below their resolution, nor that more massive star clusters could form in a single star forming event.

Here, we present a different approach. We also perform numerical simulations of isolated galaxies (i.e. no other galaxy is involved) but we distribute the newly formed stars into dissolving star clusters within a dark matter halo, which allow the formation of objects that resemble classical dSph galaxies. Our model is based on the assumption that stars never form in isolation but in hierarchical structures (i.e. star clusters) (e.g. Lada & Lada 2003; Lada, Lombardi & Alves 2010). The star formation events range from slowly forming stars in small clusters and associations to intense star-bursts, in gas-rich environments, typically producing a few to a few hundred young star clusters, within a region of just a few hundred pc (e.g. Whitmore et al. 1999).

Those star clusters form embedded inside a molecular gas cloud and eventually will expel their remaining gas via various feedback processes such as stellar winds, UV-radiation and finally the onset of supernovae (e.g. Goodwin 1997a,b; Boily & Kroupa 2003a,b; Parmentier et al. 2008; Bonnell et al. 2011; Smith et al. 2011a,b, and many more and references therein). If the star formation efficiency (SFE) is low then the star clusters are not able to form bound entities and instead they will disperse their stars and dissolve.

In this paper, we propose that the dynamical evolution of these star clusters, i.e. their dissolution due to gas expulsion, may explain the formation of classical dSph galaxies. In our scenario we simulate SCs within a DM halo, as a natural extension of the work of Fellhauer & Kroupa (2002); Wilkinson et al. (2005); Praagman et al. (2010). The star clusters form with low SFE and, thus, are designed to dissolve inside the DM halo to form the luminous component of the dSph galaxy. We follow the evolution of the star clusters within the DM halo for 10 Gyr, and then we measure the properties of the object.

In our models, we observe fossil remnants of the formation process in the velocity space of the final objects of our simulations, providing predictions for kinematic observations in the future that could test our scenario.

In the next section we explain our idea in more detail followed by Sect. 3 in which we describe the setup of our simulations. We present the results of our fiducial model in Sect. 4 and discuss them in the final section.

2 MOTIVATION

Our fiducial model is supported by two widely accepted theories. One of them is the structure formation in the Λ -Cold Dark Matter (Λ -CDM) paradigm. In this scenario galaxies form hierarchically in the potential well of DM haloes and small haloes form first. Λ -CDM cosmology with its large N-body models of the Universe (e.g. Millennium II simulation of Boylan-Kolchin et al. 2009) and the local universe around the MW (Via Lactea INCITE simulation of Kuhlen et al. 2008) predict that a galaxy like our MW should be surrounded by many of small DM haloes, which should/could host a dwarf galaxy as the luminous component.

The second theory describes the star formation inside of galaxies. It is now widely accepted that stars form in a clustered mode (e.g. Lada & Lada 2003, and follow-up publications). In extreme star bursts as in collisions of gas-rich galaxies massive star clusters or even cluster complexes, i.e. clusters of massive star clusters (e.g. the knots in the Antennae Whitmore et al. 1999) are formed. Low star formation rates form open clusters or associations, which have low SFE and are more likely to dissolve.

In our scenario we simulate the DM halo of a dwarf galaxy. In its central region, i.e. where the luminous component is formed out of the assembled baryons, we insert star clusters which have a low SFE and therefore are designed to dissolve. These star clusters orbit the central region of the halo, while they are dissolving, thereby forming the faint luminous component of the dwarf. We have to use dissolving star clusters to form the low-density luminous component, as the merging of bound star clusters will only form bound compact objects (e.g. Fellhauer & Kroupa 2002). But as the dSph galaxies are expected to only form stars with a very low star formation rate, this assumption might be justified (see e.g. Bressert et al. 2010).

dSph galaxies which show globular clusters might have formed some star clusters with a high SFE, which allowed some of them to survive and still orbit their dwarf galaxy.

We follow the evolution of the dwarf galaxy for ten Gyr and measure its properties at the end.

3 SETUP

We consider the following set-up for our simulation:

- The dark matter halo has a cusped Navarro, Frenk and White (Navarro et al. 1997) profile. Cold dark matter only cosmological simulations predict all DM haloes should follow a profile which can be approximately parameterized in that way. It is modeled using 1,000,000 particles according to the recipe described in Dehnen & McLaughlin (2005). As variable parameters we use M_{500} , the mass enclosed within 500 pc and the scale-length $R_{s,h}$ of the halo distribution. For our fiducial model, which is described in this paper $M_{500} = 10^7 M_\odot$ and the scale length is 1 kpc. Using a standard value for $H_0 = 70 \text{ km s}^{-1} \text{ Mpc}^{-1}$ and $r_{\text{vir}} = r_{200}$ leads to a virial radius of 12.7 kpc for the halo ($c = 12.7$). The value for c , i.e. the concentration parameter of the halo, falls within the predictions for dwarf haloes, which range between 5 and 20. The total mass of the halo out to the virial radius amounts to $2.3 \times 10^8 M_\odot$.

- The luminous component is initially distributed into N star clusters. For our fiducial model we use $N = 30$. This number is chosen arbitrarily. We are also running simulations with smaller (i.e. more massive SCs) and larger (less massive clusters) N and find no significant difference in our results: we are therefore confident that our results do not depend significantly on the choice of N

Table 1. Results of fitting King, Plummer and Sersic profiles to the surface density data of our four realisations of the fiducial model (The asterisk marks the simulation we discuss separately). The last line shows the fits to the three realisations we use to take a mean

number	King		Plummer		Sersic		n
	Σ_0 [$M_\odot \text{pc}^{-2}$]	R_c [pc]	Σ_0 [$M_\odot \text{pc}^{-2}$]	R_{pl} [pc]	Σ_{eff} [$M_\odot \text{pc}^{-2}$]	R_{eff} [pc]	
Sim 1	0.280 ± 0.003	410 ± 10	0.252 ± 0.001	616 ± 9	0.096 ± 0.004	500 ± 20	0.66 ± 0.03
*Sim 2	—	—	18.9 ± 0.5	61 ± 2	1.5 ± 0.3	140 ± 20	2.1 ± 0.2
Sim 3	0.326 ± 0.003	382 ± 8	0.311 ± 0.002	591 ± 9	0.103 ± 0.003	540 ± 10	0.74 ± 0.02
Sim 4	0.681 ± 0.006	231 ± 5	0.667 ± 0.006	384 ± 9	0.163 ± 0.005	450 ± 10	0.92 ± 0.02
1+3+4	0.500 ± 0.005	251 ± 6	0.490 ± 0.005	420 ± 10	0.115 ± 0.003	500 ± 10	0.94 ± 0.01

(we will present models for a range of N in Assmann et al. (2013)). It is claimed in Bressert et al. (2010) that dSph galaxies had low star-formation rate (SFR) and low SFE. Therefore, we form low mass open clusters and associations rather than massive SCs. For simplicity, we neglect the SFR and start our simulations with all N clusters forming at the same time. However, none of our conclusions in the present paper depend on the fact that all the stars in our simulations have the same age. Each SC is modeled as a Plummer sphere (Plummer 1911) using 100,000 particles (following the recipe of Aarseth et al. 1974). The SCs have a Plummer radius (half-light radius) of $R_{\text{pl}} = 4$ pc and a cut-off radius of 25 pc. This is similar to radii found for young SCs in the Antennae (Whitmore et al. 1999). We adopt a low SFE of 30 per cent and therefore the initial mass of each SC in its embedded phase is $5 \times 10^4 M_\odot$. We mimic the gas-expulsion of the SCs by artificially reducing the mass of each particle until the final mass is reached after one crossing time of the star cluster, i.e. 4 Myr. As the mass in lost gas is negligible compared to the DM mass we do not take this mass further into account. The final mass in stars (of all N clusters) after this mass loss amounts to $4.5 \times 10^5 M_\odot$, which is a typical stellar mass of one of the classical dSph (e.g. Mateo 1998). Note that this results in a particle resolution in our simulations which is slightly higher than reality, i.e. more star particles than actual stars.

- The star clusters themselves are distributed in virial equilibrium inside the halo according to a Plummer distribution. This distribution has a scale-length $R_{\text{pl, dist}}$, which in our fiducial model is 250 pc. This takes into account that we expect the stars to form mainly in and around the centre of the DM halo. As we do not know in which virial state the SCs form with respect to the halo we adopt virial equilibrium for simplicity. Also we do not take into account that the SCs might form in a disc-like structure showing angular momentum in their distribution, as we assume the gas-distribution on those small scales of a dSph rather supported by pressure than rotation. With this assumption we differ from most of the previous models in which dSph galaxies are simply the evolutionary outcome of harassed dwarf disc galaxies, which lost their angular momentum because of gravitational interactions between galaxies. Our model does not need any interactions between galaxies and therefore could explain why we see dSph galaxies in the Local Group far away from any major galaxies or any other dwarf.

We simulate the cluster complex within the dark matter halo using the particle mesh code SUPERBOX (Fellhauer et al. 2000), which has moving high-resolution sub-grids, staying focused on the star clusters. These sub-grids provide high spatial resolution at the places of interest. In SUPERBOX each simulated object has two levels of high resolution sub-grids. The highest resolution grid has a resolution (i.e. cell-length) of 67 pc for the dark matter halo and

0.8 pc for the star cluster and covers the central area of the halo or the SCs completely respectively. The medium resolution grid has a cell-length of 333 pc for the DM halo and 166.6 pc for the SCs. Finally the outermost grid covers the complete area after the virial radius of the dark matter halo with a resolution of 1.6 kpc. The time-step is fixed at 0.25 Myr to resolve the internal dynamics of the SCs.

As the SCs dissolve immediately, star particles are collisionless and two-body relaxation effects are unimportant, i.e. we are able to use a fast particle-mesh code. A particle-mesh code naturally neglects close encounters between the particles (which here are rather representations of the phase-space than actual single stars) and is therefore called collisionless. That the particles are phase-space representations makes it (in our case) possible to actually use more particles than actual stars. With the same reasoning we can model the DM halo without using an actual number of possible DM particles.

4 RESULTS

We use 30 randomly placed (according to the Plummer distribution explained above) SCs in our simulations. Some of the results may therefore suffer from this low-number under-sampling of the distribution. In other words, two realisations of the same initial conditions can lead to very different results, if the SCs are placed at different positions and different orbits, according to the same underlying distribution.

Therefore we run four different random realizations of our fiducial model and measure the radial profiles in all of the simulations. We then calculate a 'mean' profile to present in this paper. Furthermore, each simulation model may look different, when viewed from another direction, even though we simulate our models in isolation and therefore no preferred direction exists. To accommodate the fact of the unknown sight-line we calculate for each simulation the profiles as seen from three different sight-lines (along the Cartesian coordinate axes) and calculate a mean value as well. I.e. the profiles shown in this paper are not only an average over three sight-lines but also of different random realisations of the same set of parameters. With this technique we account for the effects of low-number random realisations.

We exclude one model which had a chance merger of still undisrupted SCs right at the beginning of the simulation in the centre and therefore formed a cuspy luminous profile, as the stars could not leave the deep potential well of the centre of the DM halo. All other SCs in this and all other realisations are dissolved as intended. This particular simulation shows a dSph galaxy with a nucleus. As we do not see any MW dSph with a nucleus we exclude this model

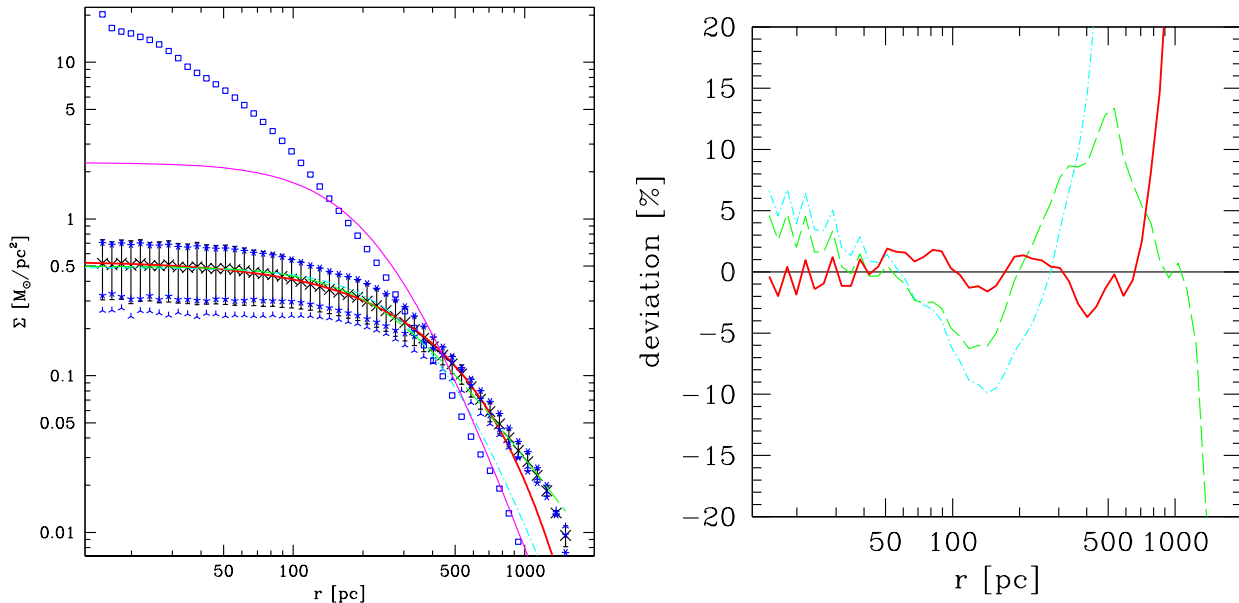


Figure 1. Left: Surface brightness profiles for the fiducial models of the dSph galaxy: The (blue) stars are realisations 1 (tri-pointed), 3 (five-pointed) and 4 (six-pointed) which we use to form the mean values. The open squares represent the results of realisation 2 which formed a central cusp, which we are not using. The data points are in themselves mean values, formed out of three different sight-lines along the Cartesian coordinate axes, as we do not know the actual orientation under which we would see the objects. The (black) crosses are the mean values with error-bars obtained out of the data-points shown from the three realisations used. The (red) solid line shows the Sersic profile fitted to the mean data, the long dashed (green) line represents a King fit without tidal radius and finally the dashed-dotted (blue) line is a Plummer fit. Finally the magenta curve shows the initial distribution of the star clusters. Right: Shows the deviation of the data points from the fitted profiles. It shows clearly that the Sersic fit represents the data best until a radius of about 700 pc.

from the calculation of the mean values but include it in the paper to show what could happen in a rare case. We emphasise that this model is not a numerical error but rather constitutes a rare event (given our initial conditions), which does not appear to have been realised with the MW dSph population we are attempting to model (with the possible exception of Sagittarius). Even though our setup for the fiducial model is tailored to have all SCs dissolving, there is still a chance that SCs survive the disruption. We will return to this issue in the follow up paper, in which we investigate a wider parameter space.

For the two-dimensional plots we focus on just one of our random realisations (No. 1).

A potentially important prediction of our model is that we need slightly less DM to explain the properties of the classical dSphs than is usually invoked. This result is already implicit from the setup section as our fiducial model is a model with only $10^7 M_{\odot}$ of DM within 500 pc, in contrast to the observational values for the classical dSph which are of the order of $10^7 M_{\odot}$ (0.5–1.5) as well, but within a radius of only 300 pc (e.g. Walker et al. 2009, their figure 4). We show in the following sections that our fiducial model does in fact match the observational data we find in classical dSph galaxies.

4.1 Surface brightness distribution

In Fig. 1 we show the surface brightness profiles of all realisations of our fiducial model. As we do not know the actual line-of-sight we take for each realisation a mean value out of the three lines-of-sight along the Cartesian coordinate axes. Furthermore and as stated before, to avoid small number statistics we plot as the large

crosses with one-sigma error-bars the mean values taken from three of our simulations (i.e. data-points are means from 3×3 values). We fit these mean values with a King, Plummer and a Sersic profile. As we do not expect a tidal radius inside a DM halo we use eq. 13 from King (1962) and fit a central surface density of $\Sigma_0 = 0.500 \pm 0.005 M_{\odot} \text{pc}^{-2}$ which translates (using a mass to light ratio for the stellar component of 1.0) into $27.2 \text{ mag arcsec}^{-2}$ and a core radius of $R_c = 251 \pm 6 \text{ pc}$. The Plummer fit leads to a central surface density of $\Sigma_0 = 0.490 \pm 0.005 M_{\odot} \text{pc}^{-2}$ and a Plummer radius (which corresponds to the half-light radius) of $R_{pl} = 420 \pm 10 \text{ pc}$. Finally, the Sersic fit

$$\begin{aligned} \Sigma(R) &= \Sigma_{\text{eff}} \exp\left(-b_n \left[\left(\frac{R}{R_{\text{eff}}}\right)^{1/n} - 1\right]\right) \\ b_n &= 1.9992n - 0.3271 \end{aligned} \quad (1)$$

gives a surface density at the effective radius of $\Sigma_{\text{eff}} = 0.115 \pm 0.003 M_{\odot} \text{pc}^{-2}$ or $28.8 \text{ mag arcsec}^{-2}$, an effective radius of $R_{\text{eff}} = 500 \pm 10 \text{ pc}$ and an index $n = 0.94 \pm 0.01$, i.e. almost an exponential profile. This matches the profiles of the classical dSph of the MW and Andromeda quite well (e.g. Irwin & Hatzidimitriou 1995; Mateo 1998), even though our models seem to be a bit on the lower luminosity side. However, this is a consequence of our chosen initial conditions, we would clearly expect higher luminosities if we insert more stars in the form of more clusters. The exact parameter values for all realisations can be found in Tab. 1.

But it is clearly visible that the final configuration of our luminous component has nothing in common with the initial set-up of our models. A Plummer profile fits not only very poorly to our model data but also has a Plummer radius of about almost twice the initial value. Furthermore, we see that our objects are well fitted by

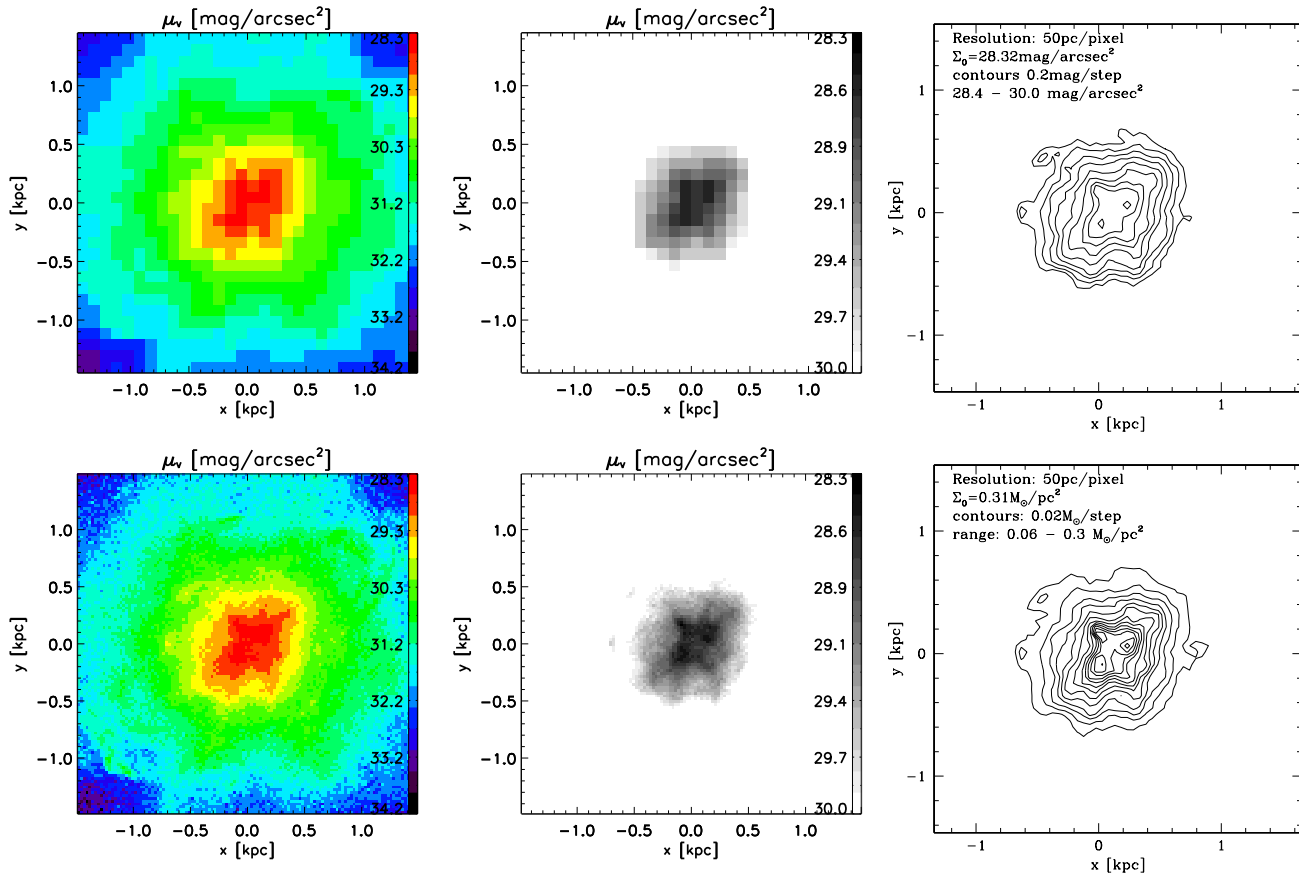


Figure 2. Two dimensional surface brightness pixel maps and contour plots of our fiducial model. The upper left and middle panels show the object with a resolution of 100 pc per pixel. The lower left and middle panels show the same model with a high resolution of 25 pc per pixel. With these two resolutions we encompass the range of resolutions of the contours produced by Irwin & Hatzidimitriou (1995), which ranges from 24 pc per pixel for Draco to 89 pc per pixel for Fornax. In the left panels we do not apply a magnitude cut and show even the faintest structures visible with our high particle resolution, i.e. in the low resolution case features ranging from 28.53 to 33.23 mag arcsec⁻² and in the high resolution case the range is from 28.32 to 34.12 mag arcsec⁻², while the middle panels show the model with a magnitude cut of 30 mag arcsec⁻² applied. The colour-bars are normalised to values between 28.3 and 34.2 (30.0 respectively) mag arcsec⁻². In the right panels we show contour plots of the fiducial model, now with an intermediate resolution of 50 pc per pixel. The top panel shows magnitude contours (logarithmic scale) while the bottom panel shows mass per pixel contours (linear scale). The lower contours are better for the comparison with Irwin & Hatzidimitriou (1995), as they plot star-counts as sigma-levels above the background (linear scale).

exponential profiles and therefore we conclude that the profile of the initial distribution is of minor influence on the final profile.

In Fig. 2, we show two-dimensional surface brightness pixel maps of the first of our simulations of our fiducial model using colour pixels (pixel values are indicated with the colour bar). In the top left panel (shown at resolution of 100 pc), we can observe a smooth object with values for the surface brightness between 28.2 and 33.5 mag arcsec⁻². In the region of very low surface brightness we see a hint of arms and spikes, which are remnants of the formation process. They are visible only because we have ideal conditions in our simulations. We do not have any foreground, background or halo star contamination and we ‘see’ all the stars of the dwarf galaxy, while observers sometimes only see the upper part of the main sequence and evolved stars (e.g. red giants). In fact our mass resolution is even better than reality as the particles in our simulations can have arbitrary mass (here less than one star) and therefore we have an over-sampling in our simulations. If we apply a magnitude cut of 30 mag arcsec⁻², roughly the intensity limit which a telescope can detect (Majewski et al. 2005) (top middle panel), we see that these faint structures disappear.

The bottom left and bottom middle panels show our dSph

galaxy with a much higher resolution of 25 pc. Here we really take advantage out of our over-sampling. Again the left panel shows even fainter structures, while the middle has a magnitude cut of 30 mag arcsec⁻².

The central part still looks rather smooth but we see hints for deviations from smooth ellipses. In the middle panel one could suspect that the actual centre of density is not in the centre of the galaxy but rather splits up into two or three components, which are slightly off-centre. Those inner structures could resemble the sub-structures of Ursa Minor as reported by Kleyna et al. (2003).

In the inner parts violent relaxation processes triggered by the cuspy DM halo have erased and smoothed out most of the features. We see in our simulations that star clusters which are on rather radial orbits spread their stars smoothly in the central region, leaving no trace of their initial orbit. Star clusters on rather circular orbits have the chance to spread their stars in ring-like structures, which may survive even after 10 Gyr. The further out these rings are, the longer is the local relaxation time and higher is the chance to observe them even after 10 Gyr. But even in the central part the dSph galaxies have very long relaxation times so some unrelaxed parts might be expected.

In the outer parts, the very-low density regions (> 30 mag arcsec $^{-2}$), where relaxation times are longer we clearly see arcs and spikes. These stem from our formation process in which some star clusters orbit out to large radii thereby slowly dissolving and losing their stars. Those arcs are clear sign of stars still moving on the former orbits of the star clusters we used to build the galaxy. In the outer parts these structures survived the 10 Gyr of evolution unharmed. We see trails similar to the ones around major galaxies which have undergone mergers. But in a dSph their surface brightness is too low to be detected with today's observations.

The choice of our resolutions represents on the high-resolution side (lower row) the resolution we have in our grid-code (actual grid-resolution is 16 pc). Furthermore with the choice of 25 and 100 pc we encompass the resolutions shown in Irwin & Hatzidimitriou (1995), which range from 24 pc per pixel for Draco to 89 pc per pixel for Fornax.

But how can we compare the results of our simulations with the actual observations of Irwin & Hatzidimitriou (1995)? In the Fornax galaxy, we would expect to detect deviations of smooth contours more easily, as Fornax has more stars and therefore sub-structures could be stronger than noise. Unluckily Fornax is far away and we do not have sufficient resolution. This might be the reason why Fornax rather looks smooth like the top-right panel of our figure. On the other hand the observations of Draco have sufficient resolution but Draco is less luminous (a factor of ten in star counts at all radii), so there are not enough bright stars to distinguish features like in our high-resolution panels from noise. Still, in fig. 1 of Irwin & Hatzidimitriou (1995) there is a hint of a deformation in the contours of Draco.

For a better comparison we include the two right panels which show contours of our model with a medium resolution of 50 pc per pixel. The top panel uses again a magnitude scale while the bottom panel has a linear mass-scale. As Irwin & Hatzidimitriou (1995) also use a linear scale (sigma-deviations of counted stars above the background) the lower right panel gives the best match to the figures in that observational paper. We see bumps and dents in the contours like we see in Carina (dents) or in Sextans (bumps). We also see that the central part has two density peaks, similar to what we see in Ursa Minor.

We calculate the 'clumpiness' of our model according to Conselice (2003):

$$C = \frac{\sum_{\text{allpix}} m_{\text{residual,pixel}}}{\sum_{\text{allpix}} m_{\text{original,pixel}}} \quad (2)$$

where the 'clumpiness' is defined as the sum of all positive fluxes from the residuals divided by the sum of fluxes of the original data. We use the IRAF routine ELLIPSE to calculate a smooth model, which we then subtract from the original data, to obtain the positive residuals.

In our model the C parameter is very low at $C = 0.045$. This again hints that the sub-structure we see in the brightness maps of our model might be only visible due to our 'larger than reality' particle resolution. The faint structures in our simulations are definitely real and not due to noise. But, once more, we have more particles in our simulation than actual stars in the dwarf galaxy and definitely a better particle resolution than observing only the brightest stars in the dSph galaxy. We therefore doubt that our formation scenario, which produces very faint sub-structure in the surface-brightness map, will be testable in the near future by purely photometric observations, counting stars in pixels. Instead we will show in a later section how our model can be verified.

Looking at the smooth image we see that both the pitch angle

Table 2. Velocity dispersion values and deviations from the mean velocity. Column one gives the number of the realisation (again the asterisk marks the simulation we single out). $\sigma_{\text{los},0}$ is the velocity dispersion in the central pixel, $\sigma_{\text{los},0,\text{fit}}$ is the central value obtained by fitting a Plummer dispersion profile to the velocity dispersion data given in Fig. 3, $\sigma_{\text{los},500}$ is the velocity dispersion of all particles within a projected radius of 500 pc and finally δ_{500} is the highest relative deviation of the mean velocity within 500 pc, using a pixel size of 20 pc.

Simulation	$\sigma_{\text{los},0}$ [km s $^{-1}$]	$\sigma_{\text{los},0,\text{fit}}$ [km s $^{-1}$]	$\sigma_{\text{los},500}$ [km s $^{-1}$]	δ_{500}
Sim 1	7.5	9.95 ± 0.07	9.0	0.68
*Sim 2	11.3	11.8 ± 0.20	14.5	0.2
Sim 3	8.4	8.95 ± 0.03	7.0	0.5
Sim 4	7.3	7.87 ± 0.05	8.3	1.7

and the shape of the ellipses vary throughout the dwarf. The pitch angle varies between -35.2 to -49.5 degrees and the ellipticity shows variations between 0.16 and 0.47, i.e. our model gets rounder in the outer parts. This again matches the ellipticities of the classical dwarfs, which are on the order of 0.3 (Irwin & Hatzidimitriou 1995).

We do not discuss the effects of the star clusters on the dark matter halo because their total mass is very small compared with the mass of the halo. In our simulations the dark matter halo remains cuspy during all the 10 Gyr of evolution. This is in accordance with the recent work of (Cole et al. 2011), as our star clusters are dissolving and therefore low-mass and low-density objects.

4.1.1 Model 2

Finally we should return to the model (number 2), which we have singled out. An inspection of the merger history of this model showed that very early in the evolution of this model a few star clusters merged in the very centre of the DM halo. Here they were not subject to dissolution due to the gas-expulsion. In reality they might have even retained their gas and formed a second generation of stars later on. In our model they lost their gas anyway (due to our gas-loss prescription). But instead of expanding to complete dissolution they sat in the centre of the deep cuspy potential well of the DM halo forming a dense nucleus. If our formation process for luminous components of galaxies is true not only for dSph but also for larger, more massive objects, this by chance result of one of our simulations could give a quite natural explanation why some dwarf ellipticals have a nucleus and some not. But this is speculation beyond the scope of this paper. In our case it only depended on the random seed and therefore where the initial star clusters were positioned. As we see no nucleated dSph galaxies in the Local Group, this could hint towards a much lower star formation efficiency and a slower star formation rate in these dwarfs than adopted in our fiducial model.

4.2 Velocity Space

In left panel of Fig. 3 we show the line-of-sight velocity dispersion profiles (σ_{los}) for our four simulations and the crosses again show the average of three of our realizations and the three Cartesian sight-lines. Even though the profiles seem to be quite below 10 km s $^{-1}$ (we see a mean central velocity dispersion of about 7.5 km s $^{-1}$) the profiles are almost flat, out to a radius of 500 pc. We see similar velocity dispersion profiles in Leo II and Sextans

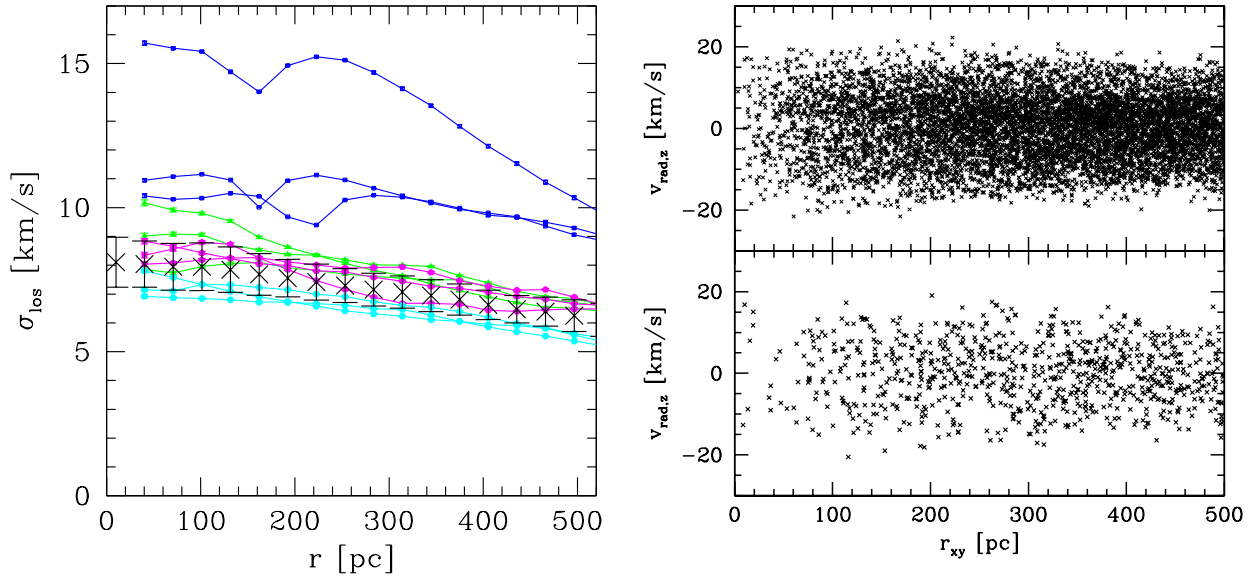


Figure 3. Left: Line of sight velocity dispersion profiles along the x -, y - and z -axis of our four fiducial models as open and closed symbols are shown (green = sim.1, blue = sim.2, magenta = sim.3, cyan = sim.4). Error-bars for the single values are smaller than the symbol-size. The mean values out of three simulations with 3 sight-lines each are shown as black crosses with error-bars (symbols as in Fig. 1). Middle: Relative deviations of the mean velocity. Shown as lines is the mean deviation of the three sight-lines, calculated in radial bins, of all four simulations (simulation 2, not used to derive the average, as dashed line) and the average thereof as the black crosses with error-bars. The velocities are divided by the velocity dispersion calculated within 500 pc: σ_{500} . Right: Radial velocity vs. radius, shown for model 1 and one sight-line. Top: one star in one hundred to show the richness of our simulation data; Bottom: one star in one thousand to mimic the best observational data available.

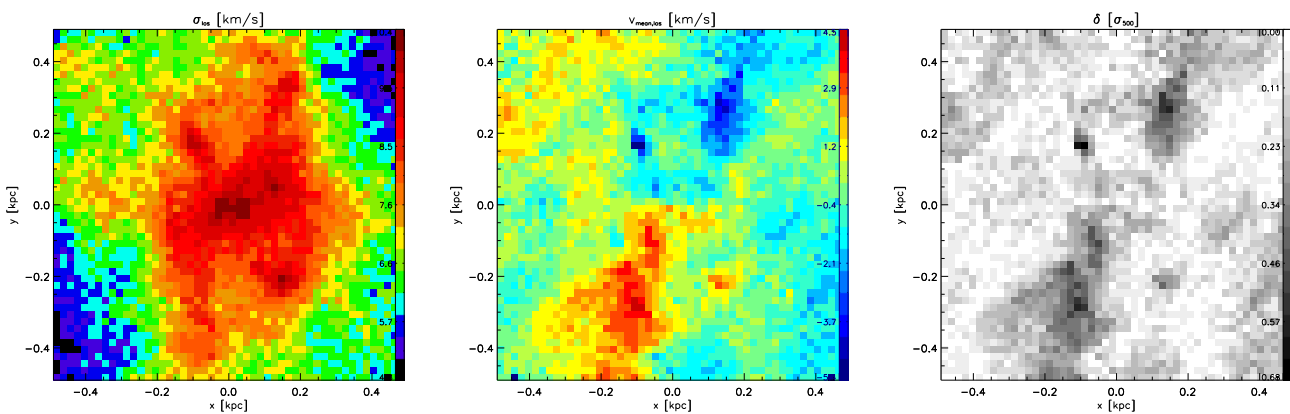


Figure 4. The 2D velocity structure of model 1. Shown is the central region out to 500 pc with a resolution of 20 pc per pixel. Left panel is a map of the velocity dispersion measured in each pixel. Middle panel shows the mean velocity map calculated for each pixel separately and finally the right shows the scaled velocity deviation, which we call δ -parameter (see main text for explanation).

(Walker et al. 2009). The lines show the dispersion profiles of each sight-line and each realisation. Here we see again mostly flat profiles but some profiles show wiggles, dips or bumps. While observers usually would have large error-bars and would use a smooth curve to fit through the data, we argue that those deviations from a smooth curve are real and due to our formation process. We also included error-bars for the data-points of the single simulations, single sight-line data-points. But these error-bars are smaller than the actual size of our small symbols as each data-point is based on 1,000 to 60,000 single velocities. In fact these wiggles and bumps

might be the only possible way, with the observations we have today, to verify our scenario. Only realisation 2 shows a very high dispersion, which we discuss in a separate section below. Again we exclude this realisation from our mean values. The results of our four realisations are also given in Tab. 2.

Finally, in the right panel of Fig. 3 we show the radial velocity of our particles of simulation 1 as function of their radius. In the top panel we show one percent of our particles to emphasise how well we are able to resolve the velocity space. The lower panel shows one particle in 1,000, which compares with the best available

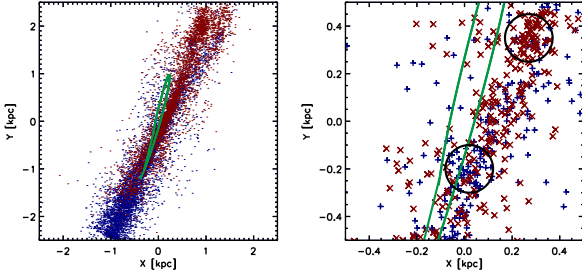


Figure 5. Orbit (green line) and particles of one dissolved star cluster. Red crosses are particles with negative velocities, blue plus-signs have positive velocities. At the right panel we see a blow up of the inner region and the circles show areas with mainly positive or mainly negative velocities.

observational data, present to date. Again, in this low-resolution plot, such as could be obtained from current observed data, we do not see a strong sign of coherent motion, even though an inspection by eye of the 'full' simulation data (upper panel) of Fig 3 would suggest some bi-modality in the very centre.

If we use all stars within a radius of 500 pc to compute an overall velocity dispersion we get $\sigma_{\text{los},500,\text{mean}} = 9 \text{ km s}^{-1}$ which resembles the values observed in classical dSphs as reported by Munoz et al. (2005); Walker et al. (2007). This mean value of the velocity dispersion velocity is calculated considering the lines-of-sight along the three coordinates, because the sight-line of the dSph galaxy towards us with respect to our formation scenario is unknown.

In Fig. 4, we show the dynamics of the first realisation within 500 pc as two-dimensional pixel maps with a resolution of 20 pc. In the left panel we show the line-of-sight velocity dispersion calculated for each pixel separately. We see regions of high velocity dispersion of more than 10 km s^{-1} in the central area but also at the locations where the off-centre density peaks are. In high resolution the distribution of dispersions is far from being smooth. In fact we see even more sub-structure than in the density plots. While the DM cusp was able to erase most of the structure in positional space, the structures in velocity space survived. We call these structures in velocity space which stem from the formation process of the dwarf 'fossil remnants'. Still we see high values of velocity dispersion throughout the visible part (surface brightness above $30 \text{ mag arcsec}^{-2}$) of the dSph galaxy.

In the middle panel we show the mean velocity of all particles within a pixel. The figure shows clearly regions which seem to exhibit coherent streaming motions with velocities differences of up to 5 km s^{-1} . This means, even after 10 Gyr of evolution we still see the stars of dissolved star clusters, which were on rather circular orbits in coherent motion. The panel shows at least two structures of opposing radial velocities. A similar scenario was proposed by Kleyna et al. (2003) to explain the velocity structure of UMi (though in the plane of the sky and therefore with no detectable offset in mean velocity).

We define a δ -parameter:

$$\delta \equiv \frac{|v_{\text{mean}}|}{\sigma_{\text{los},500}}, \quad (3)$$

where v_{mean} is the mean velocity measured in the radial bin or later in a pixel and σ_{500} is the velocity dispersion measured within a projected 500 pc radius. This parameter allows us to quantify how

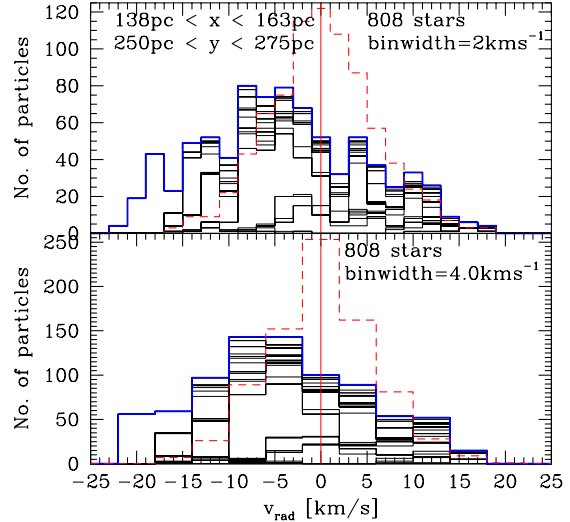


Figure 6. The right panel of Fig. 4 shows a pixel with a high $\delta = 0.44$ parameter in the upper right part. Here we show the radial velocity histogram of all 808 particles in this pixel as the solid (blue) histogram. In the top panel we bin the data with 2 km s^{-1} bins and in the lower panel we show the same data with a bin-width of 4 km s^{-1} . For comparison, the dashed (red) histogram shows a distribution of 808 randomly chosen particles throughout the dwarf. The thin black histograms within the solid blue one show the cumulatively summed histograms of the particles from the 30 different star clusters added one after the other

strong coherent motions in the object are. The function δ corresponds to a re-normalization of the mean velocities, which allows to see easily regions where the mean velocities are distinct from zero. Higher values of δ correspond to regions where streaming motions and/or rotation are present.

While the value of the δ -parameter depends on the strength of the velocity deviations in our model, the significance of those values, i.e. if they could be due to noise in the data-sample, depend on the number of velocities in the sample. If we would apply a strict criterion to regard only the deviations which have δ -values higher than possible 3σ -deviations (due to noise) as real, then we have to have values larger than 1.25, 0.39 and 0.14 for sample sizes of 10, 100 and 1000 stars respectively. For more detailed values see table 1 in Fellhauer (2011).

The right panel shows the δ -parameter. If no streaming motion is present we expect the δ values to be randomly distributed without correlation. As our high resolution plots have more than 300 and up to 3000 particles in each pixel, the δ values we see of up to 0.68 are definitely significant and not due to noise produced by low particle numbers.

We speculate above that our fossil remnants could be related with star clusters which dissolved on rather circular orbits. In Fig. 5 we show the particles of one of our dissolved clusters. Its initial orbit is shown as a green line on top of the particles, which got spread out to much larger distances than the original orbit. Still they form a ring-like structure, where at the upper end of the ring are more particles with negative velocities, while at the lower end we see particles with positive velocities. But the 'ring' is too large for its ends to be the explanation of the two places of high delta values we see in the right panel of Fig. 4 (top right and lower left area). If we zoom in (right panel), we see that even though the ring

is much larger there are areas where the particles of this dissolved cluster have predominantly positive or negative velocities (circles). These areas coincide with the pixels of high delta values.

In Fig. 6 we focus now on one pixel with a relatively high δ -value of 0.44. It is located in the upper right area of Fig. 4. We plot the histogram of radial velocities of all 808 particles in this pixel (taken from all dissolved SCs, including the one we show in Fig. 5). The top histogram, which has a good resolution of 2 km s^{-1} , shows that we have a complicated structure with several peaks and that the majority of particles have negative velocities. If we fit a Gaussian to this data we obtain a mean value of $-4.7 \pm 0.3 \text{ km s}^{-1}$ and a $\sigma = 9.4 \pm 0.3 \text{ km s}^{-1}$ (skewness: 0.202; kurtosis: 2.354). If we would have a 'normal' non-rotating velocity distribution, the mean value has to be zero and the velocity dispersion reflects the strength of the potential according to the Jeans equation. In reality, our histogram reflects many different streams of particles from many different dissolved star clusters rather than a smooth distribution of a uniform object in virial equilibrium. Therefore, the peak is shifted and the 'measured' velocity dispersion is much higher than expected. This is clearly visible if we look at the cumulative histograms of the different dissolved star clusters, which are shown as the thin, solid lines (black) in Fig. 6. Larger areas without lines show where some star clusters deposit a lot of stars, i.e. we have a stream of stars from that particular cluster inside this pixel. We also see that we do not have 30 large areas inside this pixel, i.e. we do not find stars from every cluster in this pixel.

This reflects the complicated velocity structure we have throughout the dwarf galaxy. The particles of the different SCs are not distributed evenly and smoothly throughout the whole available phase-space. Some of them still occupy distinct regions, reflecting the former orbit of the SC they came from.

The better the resolution is, with which we view the object (smaller areas, larger particle samples) the more visible are these structures. In the lower panel we plot the same velocity sample with half the resolution and the complicated multi-peak structure disappears, only the shifted mean and the large σ -value remain.

If we sample the same amount of velocities randomly from all over the dwarf (red, dashed histograms in Fig. 6) the distribution is indistinguishable from a normal Gaussian (skewness: 0.055; kurtosis: 3.305). The mean value is centred on zero (0.06 ± 0.09) and $\sigma = 5.35 \text{ km s}^{-1}$ (Remember, we sample from the whole object, i.e. also from the very outer parts showing low dispersions; the velocity dispersion of all particles within 500 pc is still $\sigma_{500} = 9.0 \text{ km s}^{-1}$).

The result of these complicated velocity structures or 'fossil remnants' as we dub them is that we could see regions with high velocity dispersion and regions with deviations in mean velocity, if we have high enough resolution, i.e. having both: small pixel size and still enough stellar velocities per pixel. If we do not have the necessary resolution we still could see bumps and wiggles in the velocity dispersion profiles and we might observe a velocity dispersion that is enhanced relative to the equilibrium value for a smooth model. If we use the Jeans equations to estimate the mass of the system we could then be biased to larger values of the mass.

4.2.1 Model 2

Again we have to discuss our singled out model separately. Fig. 3 shows that this model exhibits a 'cold' core with a rising velocity dispersion outside the nucleus, reaching up to 13.5 km s^{-1} and dropping again to values similar to the other random realisations. As said in the previous section, this simulation exhibits a nucleus, which we do not find in the known dSph galaxies of the MW. But

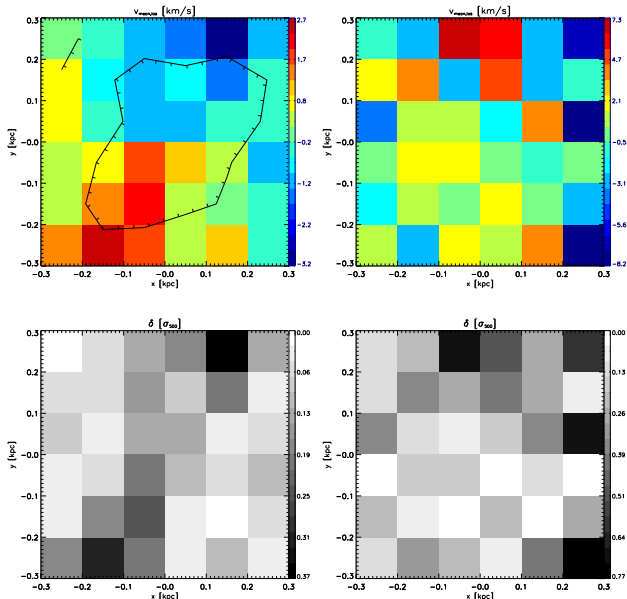


Figure 7. Contours with a very low resolution of 100 pc per pixel showing mean velocity in the top row and δ -parameter in the bottom row. The left side is our model data and the right side is based on radial velocities measured in the Fornax galaxy. The large velocity sub-structure in our model (top left panel), overlaid with black contours can easily be mistaken for an indication of rotation or a velocity gradient along the major axis. See discussion in the main text.

as expected for a nucleus inside a prominent DM halo we see a dip in the velocity dispersion. The maximum in the dispersion is due to the fact that in this particular model quite a lot of the luminous mass got trapped in the nucleated centre instead of being more distributed like the other models.

4.3 Comparing our model with dynamical observations of Fornax

We try to compare our model with the available Fornax data in Fig. 7. The top left panel shows the velocity differences of the central part of our model with a resolution of 100 pc per pixel. Overlaid is a contour of the surface brightness. Within this contour the velocity structure could be mistaken as a signal of rotation around the minor axis or a velocity gradient of about 5 km s^{-1} . Underneath we see that the pixels showing the strongest deviation have a δ -parameter of about 0.5. Now with our particle resolution we have more than 10,000 velocities in each pixel and we can be sure that this velocity structure is real and not due to noise. Still, with this low resolution most signals of our complicated velocity structure are erased. The biggest structure is just visible in the top panel due to a dark red and a dark blue pixel and in the bottom panel through one dark pixel on either side of the object. We conclude therefore, that having only low resolution one cannot see coherent motions (several pixels together showing the same behaviour) but rather has to search for symmetric pixels with high deviations.

On the right hand side we try to produce a similar figure of the inner part of Fornax. Fornax has almost 2,000 radial velocities publicly available. In the region printed we have about 800 velocities. Still, we have just around 20 velocities per pixel (minimum value: 8) even with pixels this large. There are pixels which show high deviations in the mean velocity but first of all the strength of these

deviations is still within the possible noise (about a one-sigma deviation from the system velocity, a 3σ -deviation due to noise would result in delta values of 1.25 for ten stars or 0.91 for 20 stars) and second we cannot detect any symmetry between the pixels with high values. So we have to conclude that the presently available data of Fornax does not show any visible fossil remnant, as we do not have sufficient data to disentangle possible sub-structure in velocity space from the possible level of noise.

Once again: even though our model and Fornax show deviations from the systemic velocity of the same strength, in our model these deviations are well above any noise and show symmetries, while Fornax lacks sufficient data to enhance any structure, if present, above the possible level of noise. If we would degrade our data to the same low resolution in pixel size *and* particle sampling, as available for Fornax, not a single fossil remnant would remain visible above the noise level.

5 DISCUSSION

In this section we discuss in more detail the observational detectability in real dSphs of the features we have seen in our simulation.

If we analyse Fig. 2 in terms of detectability we find that the visible sub-structure in the surface brightness (bottom left panel) amounts to tiny differences in actual mass-densities. Within a 20×20 pc pixel the difference between the dark red and red pixels amounts to a difference of about $20 M_{\odot}$. In our simulations we can easily resolve such mass differences. In reality, regarding the fact that most of this mass-difference will be in faint low-mass stars, which are hard to detect at the distance of the dSph galaxies even with modern telescopes, these sub-structures will be below the detection limit. Maybe the next generation telescopes like E-ELT, TMT or GMT will be able to make those structures visible.

But effects like slightly off-centre nuclei (Sextans), secondary density peaks (Ursa Minor) or dents in the contours (Draco) (as seen in Irwin & Hatzidimitriou (1995)) are now potentially explainable with our scenario as low-resolution counterparts of a more complicated structure due to the formation process.

Looking at the velocity dispersion profiles of our fiducial models, we find similar radial profiles to some of the classic dwarfs of the MW. If we recall the profiles of the different realisations of our standard model in Fig. 3 we see that some of them show not only an almost flat profile but also bumps or dents. In our simulations these deviations from a smooth curve are not due to noise (as we have 1,000 to 60,000 velocities in one bin) but are intrinsic deviations stemming from our formation scenario. They are hints to the fact that a more complicated velocity structure exists in our model. In reality (Walker et al. 2009) we see similar bumps in Carina, Leo I and Sculptor, even though the observational error-bars are still much larger than the deviations.

Even though some of the classical dwarfs have now more than 2,000 radial velocities, it is still not feasible to produce 2D velocity maps of the dispersion or the mean velocity with a sufficiently high resolution to detect 'fossil remnants', as we see in Fig. 7 where we compare our simulations with Fornax data set. If with next generation telescopes several thousands of radial velocities more for each dSph galaxy would become available, significant sub-structure in velocity space might emerge above the expected level of noise. In our fiducial model we found a maximum δ -value of 0.4, if we degrade our resolution to a pixel-size of 100 pc. In order for this feature to be detectable above the noise at a statistically significant

level, we would need at least 100 velocities per pixel (to be above a 3σ noise level).

Another interesting property of our model is that if you would draw an imaginary line along the maximum extension of our object in surface brightness (red/orange area in the left panels of Fig. 2 or grey area in the middle panels of the same Figure, i.e. the projected major axis), the position angle of this line would be different to a similar line drawn through the maximum extension of high velocity dispersion (red/orange area in the left panel of Fig. 4). Furthermore, a line through the two regions of high mean velocity deviations (blue and red area in the middle panel of Fig. 4 or two main dark areas in the right panels of the same Figure), again would show a different position angle. In other words, if one would fit ellipses of constant surface brightness and constant velocity dispersion to our data shown in Fig. 2 and Fig. 4 (left panel), their position angles would differ. Furthermore, searching for the position angle along which we see the highest velocity gradient in our data (middle panel of Fig. 4), this angle would differ from the other two. This is something which might only occur in our formation scenario and therefore would be a measurable quantity. Unluckily, a perfect alignment would not exclude our scenario. Just a perfect alignment in all known dwarfs would render our scenario very unlikely.

One important ingredient of our models is the low SFE and therefore the subsequent dissolution of the SCs. Only with the dissolution of the SCs we are able to lower the phase space density of the stars sufficiently to obtain low luminosity objects like dSph galaxies. Merging SCs without expansion always lead to compact objects, even without the presence of a DM halo (Fellhauer & Kroupa 2002). We see the difference in our model 2, which had a chance merger early on in the centre, thereby preventing the merged SCs from dissolving. As such objects as model 2 are not observed, we could conclude that the SCs which formed the known dSph had even lower SFEs and slower SFR than adopted in our model.

Last but not least, this paper only talks about our fiducial model, i.e. one particular set of parameters that without much tweaking results in an object which resembles (as shown in the section above) a classical dwarf spheroidal galaxy in terms of appearance, scale-length and velocity dispersion (without matching one particular dwarf of the MW in every aspect). A thorough investigation of the vast possible parameter space (M_{500} , $R_{\text{scale,halo}}$, $R_{\text{scale,SC}}$, shape of the DM halo, distribution and virial ratio of the SCs,...) will be dealt with in the follow-up papers we wish to publish.

Finally, one should bear in mind that after all, our model is still a toy model making a lot of simplifications (all SCs form at the same time, have the same mass and SFE, gas is lost entirely from the system,...), some justified, some because we have no better knowledge. Also here we have to investigate a much larger parameter space, which we will do in the future. A somewhat delayed formation of some of the SCs might be a plausible explanation of the spread in metallicity we see in dSph galaxies. If not, a low SFR with low SFE also implies that we will lack high-mass stars and strong super-nova explosions (Weidner et al. 2010) which might be able to blow the remaining gas out of the DM halo. Retaining the gas could then lead to another epoch of star formation later on.

6 CONCLUSIONS

In this paper we tested a possible scenario for the formation of dSph galaxies with numerical simulations using the particle mesh code

SUPERBOX. In our simulations we considered the evolution of $N = 30$ star clusters within a dark matter halo with an NFW profile. We observe that these star clusters dissolve due to the low SFE = 0.3 assumed and form an extended luminous object which resembles a dSph galaxy and after 10 Gyr of evolution has a projected diameter of about 1 kpc.

One major result to take away from our models is that even 10 Gyr of evolution is not enough to erase sub-structures stemming from our formation process inside of the dSph. These substructures are mainly visible in velocity space. Because of these substructures, i.e. coherent motions, the measurements of the velocity dispersion of the object may be affected. For this reason our fiducial model can mimic the observations of a classical dSph galaxy even within a halo that only has $M_{500} = 10^7 M_{\odot}$, a value somewhat lower than the canonical values M_{300} (Strigari et al. 2008; Walker et al. 2009) obtained by using the measured velocity dispersion and assuming complete virial equilibrium without coherent motions.

The external structural remnants of the formation process in our model are very faint, too faint to be observed in current data sets. The central structures which are within 500 pc, have observable luminosities comparable to the luminosity of the dSph galaxies of the MW. But the sub-structures stemming from the formation process visible in the two-dimensional brightness distribution of our model are only visible through our ultra-high particle resolution and are currently unobservable, as long as we cannot see all the stars of the dwarf. If such structures are present, only future telescopes like the E-ELT might be able to observe them.

Still, those structures have low-resolution counterparts in off-centre nuclei, secondary density centres and oddly shaped contours, as present in some of the dSph galaxies we know.

In velocity space the object has the overall properties of a typical classical dSph galaxy. We show that the velocity dispersion of this object is around 10 km s^{-1} and that it has a flat velocity dispersion profile in projection. Again this resembles closely the observations of the known classical dwarfs.

Besides we show the existence of streaming motions in this object even after 10 Gyr of evolution. These streams are fossil remnants of the dissolving star clusters considered in our simulations, mainly of those with more circular orbits. As mentioned above these kinematical sub-structures only become visible in high-resolution pixel-maps. The current state of the art measurements in real dSph galaxies using up to and more than 2,000 velocities in total is astonishing but do still not give enough resolution to find those fossil remnants, predicted by our model, in reality. Our model showed one strong fossil remnant, which might be detectable in real observations possible today. This structure is still visible if we reduce our resolution to a resolution possible with present day observational data. It might be an explanation for the ring-like structure suspected in UMi or it could be easily mistaken as a velocity gradient throughout the luminous component, as for example observed with UMa II and Her.

It is important to note that these structures have 1D counterparts. We see in the dispersion profiles dents and bumps. In our simulations these are not errors of the measurement but real features. The same behaviour is visible in some of the MW dSph galaxies. In observational papers these dents or bumps are smoothed over because the data-points have much larger error-bars but according to our scenario some of them could be real.

Our simulations show that our new scenario for the formation of dSph galaxies, joining two basic astronomical principles, indeed works. We are not only able to reproduce the observational data we have today, but our models also provide observers with predictions

for future high-precision and high-resolution observations.

Acknowledgments: PA wishes to thank W. Dehnen for his help with the NFW profiles. M. Metz for his support with Superbox. PA gratefully acknowledges support from a CONICYT PhD studentship, MECESUP FMS0605, FONDAF no. 15010003, BASAL CATA grant PFB-06/2007, FONDECYT no. 1100540 and FONDECYT no. 3130653. MF acknowledges financial support through FONDECYT grant no. 1095092 and BASAL. MIW acknowledges the Royal Society for support. RS is funded through a Comite Mixto grant and FONDECYT no. 3120135.

REFERENCES

- Aarseth S.J., Henon M., Wielen R. 1974, *A&A*, 37, 183
 Assmann P., Fellhauer M., Wilkinson M.I., Smith R., Blaña M. 2013, *MNRAS* submitted
 Belokurov V., Zucker D.B., Evans N.W., Wilkinson M.I., Irwin M.J., Hodgkin S., Bramich D.M., Irwin J.M., Gilmore G., Willman B., Vidrih S., Newberg H.J., Wyse R.F.G., Fellhauer M., Hewett P.C., Cole N., Bell E.F., Beers T.C., Rockosi C.M., Yanny B., Grebel E.K., Schneider D.P., Lupton R., Barentine J.C., Brewington H., Brinkmann J., Harvanek M., Kleinman S.J., Krzesinski J., Long D., Nitta A., Smith J.A., Snedden, S.A. 2006, *ApJ*, 647, L111
 Belokurov V., Zucker D.B., Evans N.W., Kleya J.T., Koposov S., Hodgkin S.T., Irwin M.J., Gilmore G., Wilkinson M.I., Fellhauer M., Bramich D.M., Hewett P.C., Vidrih S., De Jong J.T.A., Smith J.A., Rix H.-W., Bell E.F., Wyse R.F.G., Newberg H.J., Mayeur P.A., Yanny B., Rockosi C.M., Gnedin O.Y., Schneider D.P., Beers T.C., Barentine J.C., Brewington H., Brinkmann J., Harvanek M., Kleinman S.J., Krzesinski J., Long D., Nitta A., Snedden, S.A. 2007, *ApJ*, 654, 897
 Boily C.M., Kroupa P. 2003a, *MNRAS*, 338, 665
 Boily C.M., Kroupa P. 2003b, *MNRAS*, 338, 673
 Bonnell I.A., Bate M.R., Vine S.G. 2003, *MNRAS*, 343, 413
 Bonnell I.A., Smith R.J., Clark P.C., Bate M.R. 2011, *MNRAS*, 410, 2339
 Boylan-Kolchin M., Springel V., White S.D., Jenkins A., Lemson G. 2009, *MNRAS*, 398, 1150
 Bressert E., Bastian N., Gutermuth R., Megeath S.T., Allen L., Evans N.J.II, Rebull L.M., Hatchell J., Johnstone D., Bourke T.L., Cieza L.A., Harvey P.M., Merin B., Ray T.P., Tothill N.F.H. 2010, *MNRAS*, 409, L54
 Cole D., Dehnen W., Wilkinson M.I. 2011, *MNRAS*, accepted
 Conselice C.J. 2003, *ApJS*, 143, 1
 Dehnen W., McLaughlin D.E. 2005, *MNRAS*, 363, 1057
 D’Onghia E., Besla G., Cox T., Hernquist L., 2009, *Nature*, 460, 605
 Fellhauer M., Kroupa P., Baumgardt H., Bien R., Boily C.M., Spurzem R., Wassmer N. 2000, *New Ast.*, 5, 305
 Fellhauer M., et al. 2008, *MNRAS*, 385, 1095
 Fellhauer M. 2011, *BAAA*, 54, 155
 Fellhauer M., Kroupa P. 2002, *MNRAS*, 330, 642
 Geha M., Willman B., Simon J.D., Strigari L.E., Kirby E.N., Law D.R., Strader J. 2009, *ApJ*, 692, 1464
 Gnedin O. Y., Hernquist L., Ostriker J.P., 1999, *AJ*, 514, 109
 Goodwin S.P. 1997a, *MNRAS*, 284, 785
 Goodwin S.P. 1997b, *MNRAS*, 286, 669
 Grebel E. K., Gallagher III J. S., Harbeck D., 2003, *AJ*, 125, 1926
 Irwin M., Hatzidimitriou D. 1995, *MNRAS*, 277, 1354

- Kleyna J.T., Wilkinson M.I., Evans N.W., Gilmore G. 2001, *APJ*, 563, L115
- Kleyna J.T., Wilkinson M.I., Evans N.W., Gilmore G., Frayn C., 2002, *MNRAS*, 330, 792
- Kleyna J.T., Wilkinson M.I., Gilmore G., Evans N.W. 2003, *APJ*, 588, L21
- Kleyna J.T., Wilkinson M.I., Evans N.W., Gilmore G. 2004, *MNRAS*, 354, L66
- King I. 1962, *AJ*, 67, 471
- Koch A., et al. 2009, *ApJ*, 690, 453
- Koposov S.E., Gilmore G., Walker M.G., Belokurov V., Evans N.W., Fellhauer M., Gieren W., Geisler D., Monaco L., Norris J.E., Okamoto S., Penarrubia J., Wilkinson M., Wyse R.F.G., Zucker D.B. 2011, *ApJ*, 736, 146
- Kuhlen M., Diemand J., Madau P., Zemp M. 2008, *Journal of Physics: Conference Series*, Vol. 125, Issue 1, p.1
- Lada C.J., Lada E.A., 2003, *ARA&A*, 41, 57
- Lada C.J., Lombardi M., Alves J.F. (2010), *ApJ*, 724, 687
- Lokas E.L., 2009, *MNRAS*, 394L, 102L
- Mayer, L., Kazantzidis S., Mastroiero C., Wadsley J., 2007, *Nature*, 445, 738
- Majewski S., Frinchaboy, P.M., Kunkel W.E., Link R., Munoz R.R., Ostheimer J.C., Palma C., Patterson R.J., Geisler D. 2005, *AJ*, 130, 2677
- Mateo M.L. 1998, *ARA&A*, 36, 435
- Metz M., Kroupa P., Jerjen H., 2007, *MNRAS*, 374, 1125
- Munoz R.R., Frinchaboy, P.M., Majewski S., Kuhn J.R., Chou M., Palma C., Sohn S.T., Patterson R.J., Siegel M.H. 2005, *APJ*, 631, L137
- Munoz R.R., Frinchaboy, P.M., Majewski S., Kuhn J.R., Chou M., Palma C., Sohn S.T., Patterson R.J., Siegel M.H. 2006, *APJ*, 649, 201
- Navarro J.F., Frank C.S., White S.D.M. 1997, *ApJ*, 490, 493
- Parmentier G., Goodwin S.P., Kroupa P., Baumgardt H. 2008, *ApJ*, 678, 347
- Plummer H.C. 1911, *MNRAS*, 71, 460
- Praagman A., Hurley H., Power C., 2010, *New Astronomy*, 15, 46
- Read J. I., Pontzen A. P., Viel M., 2006, *MNRAS*, 371, 885
- Revaz Y., Jablonka P., Sawala T., Hill V., Letarte B., Irwin M., Battaglia G., Helmi A., Shetrone M.D., Tolstoy E., Venn K.A. (2009), *A&A*, 501, 189
- Sawala T., Scannapieco C., Maio U., White S. 2010, *MNRAS*, 402, 1599
- Simon J.D., Geha M., Minor Q.E., Martinez G.D., Kirby E.N., Bullock J.S., Kaplinghat M., Strigari L.E., Willman B., Choi P.I., Tollerud E.J.; Wolf J. (2011), *ApJ*, 733, 46
- Simon J.D, Geha M., 2007, *ApJ*, 670, 313
- Smith R., Slater R., Fellhauer M., Goodwin S.P., Assmann P. 2011a, *MNRAS*, 414, 3036
- Smith R., Fellhauer M., Goodwin S.P., Assmann P. 2011b, *MNRAS*, in press
- Strigari L. E., Bullock J. S., Kaplinghat M., Simon J. D., Geha M., Willman B., Walker M. G. 2008, *Nature*, 454, 1096
- Valcke S., de Rijcke S., Dejonghe H. 2008, *MNRAS*, 389, 1111
- Walker M.G., Mateo M., Olszewski E.W., Gnedin O.Y., Wang X., Bodhisattva S., Woodroffe M. 2007, *ApJ*, 667, L53
- Walker M.G., Mateo M., Olszewski E.W., Peñarrubia J., Evans N.W., Gilmore G. (2009), *ApJ*, 704, 1274
- Walsh S.M., Jerjen H., Willman B. 2007, *ApJ*, 662, L83
- Weidner C., Kroupa P., Bonnell I.A.D. 2010, *MNRAS*, 401, 275
- Whitmore B.C., Zhang Q., Leitherer C., Fall S.M., Schweizer F., Miller B.W. 1999, *AJ*, 118, 1551
- Wilkinson M.I., Kleyna J.T., Evans N.W., Gilmore G.F., Grebel E.K., Koch A., Read J., Young R. 2005, *IAUC* 198, eds. H. Jerjen and B. Bingelli
- Willman B., Dalcanton J.J., Martinez-Delgado D., West A.A., Blanton M.R., Hogg D.W., Barentine J.C., Brewington H.J., Harvanek M., Kleinman S.J., Krzesinski J., Long D., Neilsen E.H.Jr., Nitta A., Snedden S.A. 2005, *ApJ*, 626, L85
- York D.G., et al. 2000, *AJ*, 120, 1579
- Zucker D.B., Belokurov V., Evans N.W., Wilkinson M.I., Irwin M.J., Sivarani T., Hodgkin S., Bramich D.M., Irwin J.M., Gilmore G., Willman B., Vidrih S., Fellhauer M., Hewett P.C., Beers T.C., Bell E.F., Grebel E.K., Schneider D.P., Newberg H.J., Wyse R.F.G., Rockosi C.M., Yanny B., Lupton R., Smith J.A., Barentine J.C., Brewington H., Brinkmann J., Harvanek M., Kleinman S.J., Krzesinski J., Long D., Nitta A., Snedden S.A. 2006, *ApJ*, 643, L103